Multicomponent and multiphase modeling and simulation of reactive wetting

Walter Villanueva,[1,*] Klara Grönhagen,[2] Gustav Amberg,[1] and John Ågren[2]
[1]*Linné Flow Centre, Department of Mechanics, Royal Institute of Technology, SE-100 44 Stockholm, Sweden*
[2]*Department of Materials Science and Engineering, Royal Institute of Technology, SE-100 44 Stockholm, Sweden*
(Received 16 April 2007; revised manuscript received 31 March 2008; published 28 May 2008)

A multicomponent and multiphase model with fluid motion is developed. The model is used to study reactive wetting in the case where concentration change of the spreading liquid and the substrate occurs. With the introduction of a Gibbs energy functional, the governing equations are derived, consisting of convective concentration and phase-field equations which are coupled to the Navier-Stokes equations with surface tension forces. The solid substrate is modeled hydrodynamically with a very high viscosity. Arbitrary phase diagrams, surface energies, and typical dimensionless numbers are some input parameters into the model. An axisymmetric model with an adaptive finite element method is utilized. Numerical simulations were done revealing two stages in the wetting process. First, the convection-dominated stage where rapid spreading occurs. The dynamics of the wetting is found to match with a known hydrodynamic theory for spreading liquids. Second, the diffusion-dominated stage where we observed depression of the substrate-liquid interface and elevation of the contact line region.

DOI: 10.1103/PhysRevE.77.056313 PACS number(s): 47.70.−n, 02.70.−c, 47.50.Cd, 47.55.N−

I. INTRODUCTION

Many technological processess involve the spreading of a molten material over a solid substrate. Typical examples include liquid phase sintering, and soldering or brazing of ceramics. The dynamics of the wetting is an important aspect, and the final outcome of the microstructure could be largely affected whether the spreading is reactive or nonreactive.

Reactive wetting involves a chemical change and/or diffusion of chemical species. There are two cases: (i) a concentration change of the spreading liquid and the substrate occurs, and (ii) a new phase or phases form between the liquid and the substrate. Braun *et al.* [1] presented a lubrication theory for reactive spreading of a thin drop. They applied equations governing the velocity, temperature, and concentration fields in the drop and the height of the drop is an unknown variable. In addition, the contact line was assumed to move according to a known hydrodynamic law for nonreactive spreading of liquids. Warren *et al.* [2] also presented a model for the first case of reactive wetting. They used a diffusion or fluid flow analysis to predict the change in shape of the liquid-solid interface. The motion of the triple line along the substrate is driven by concentration gradients and geometrical considerations. Their simulation results showed the depression of the substrate-liquid interface, which is similar to the experiment they and other researchers have performed [3] and to the molecular dynamics simulations done by Webb and Grest [4]. More recently, Yin *et al.* [3] studied experimentally the first case in the Bi-Sn system. Their results showed certain similarities to a universal correlation for partially nonreactive wetting systems.

The second case was studied experimentally by Landry *et al.* [5] and focused on the dynamics of reactive wetting, specifically on the question of surface energy parameters determining the final equilibrium contact angle in reactive liquid-solid systems. In the work of Kalogeropoulou *et al.* [6] on Ag spreading on SiC, their results showed that the final equilibrium contact angle is characteristic of the reaction product (graphite) and not of the initial substrate, where in this case the contact angle on the reaction product is higher than the contact angle on the substrate. Thus, they argued that reactivity does not necessarily promote spreading. Another interesting experimental observation is the development of a ridge at the triple line in the systems studied by Saiz *et al.* [7,8].

The wetting phenomena can be viewed as a free boundary problem where the interface between the two fluids is deformable and free to change its shape in order to minimize the surface energy. The problem can be modeled with sharp-interface or diffuse-interface methods. Some common sharp-interface methods include the front-tracking [9], level set [10], and the volume-of-fluid method [11]. Diffuse-interface methods consider the interface between the two fluids to have a nonzero thickness endowed with physical properties such as surface tension. For a review of diffuse-interface models applied to different interfacial phenomena, see [12]. Phase-field models are a particular type of diffuse-interface models that are based on the free energy as a function of state variables, an idea that can be traced to van der Waals [13]. One notable feature of such models is that the force singularity arising in the classical model of moving contact lines as pointed out by Huh and Scriven [14] is no longer present due to mass transfer across the interface (for details see Seppecher [15]).

Different diffuse-interface models such as phase-field models for multiphase systems controlled by diffusion have been proposed by a number of workers. For example, a polycrystalline binary model was developed by Chen *et al.* [16] using a Ginzburg-Landau polynomial for the free energy. Polycrystalline binary systems in general have been modeled by many researchers [17–19]. Grafe *et al.* [20] extended the binary system to a multicomponent system. Instead of representing every grain and/or phase with a phase-field variable, Warren *et al.* [21] developed a polycrystalline model by in-

*walter@mech.kth.se.

troducing an order parameter representing a rotation of the crystallographic orientation of a grain. Garcke *et al.* [22] presented a nonisothermal phase-field model for alloys with multiple components and phases without convection. They discussed possible choices for the gradient and bulk energies in the free energy density and related their model to classical sharp interface models. With these models, numerical simulations of moving grain boundaries, triple junctions, and phase transformations can be performed. A phase-field model that includes fluid flow has been proposed by Nestler *et al.* [23] to simulate solidification of a monotectic alloy with convection. Sekerka *et al.* [24] also developed a phase-field model for solidification of a multicomponent system including fluid motion, treating the solid phase as very viscous. For reviews of phase-field models, see [25,26].

In this paper, we present a multicomponent and multiphase model with fluid motion to study the first case of reactive wetting; that is, a change in concentration between the spreading liquid and the substrate occurs without forming a new phase between them. More specifically, we model the case of sitting droplets [2,3] as opposed to running droplets demonstrated in nonmettalurgic systems [27–29]. The model is based on our previous work [30,31]. The system consists of three substitutional elements and three phases. With the introduction of a Gibbs energy functional, the governing equations are derived, consisting of convective composition and phase-field equations which are coupled to the Navier-Stokes equations with surface tension and gravity forces. The solid substrate is modeled as a liquid with very high viscosity. This allows for the deformation of the substrate-liquid interface as a result of the kinetics involved in reactive wetting. The system is nondimensionalized and typical dimensionless parameters are identified, namely, the Reynolds number Re, Capillary number Ca, Bond number Bo, Péclet number Pe, etc. Similar to [22], our model also allows for arbitrary phase diagrams as well as surface energies.

The present paper is organized as follows: In Sec. II, we formulate the governing equations and a dimensionless system is derived. Next, a numerical treatment of the system of equations is discussed followed by a discussion of the choice of parameters. In Sec. V, results are presented and the influence of surface energies, initial compositions, etc., to the dynamics of the wetting process is discussed.

II. MATHEMATICAL FORMULATION

The total Gibbs energy G of a ternary system (see Fig. 1) of substitutional elements A, B, and C with three phases, α (spreading liquid), β (substrate), and γ (medium) is given by

$$G = \int_{\Omega} \left(\frac{G_m(x_A, x_B, x_C, \phi_\alpha, \phi_\beta, \phi_\gamma, T)}{V_m} + \sum_{i=\alpha,\beta,\gamma} \frac{\epsilon_i^2}{2} (\nabla \phi_i)^2 \right) d\Omega, \tag{1}$$

where V_m is the molar volume and $x_{A,B,C}$ is the mole fraction of A, B, C atoms with $x_A + x_B + x_C = 1$. Also, ϕ_i's are phase-field variables with $\phi_\alpha + \phi_\beta + \phi_\gamma = 1$ and vary smoothly between 0 and 1, ϵ_i's are coefficients related to the thicknesses and surface tensions of the interfaces, and G_m denotes the molar Gibbs energy,

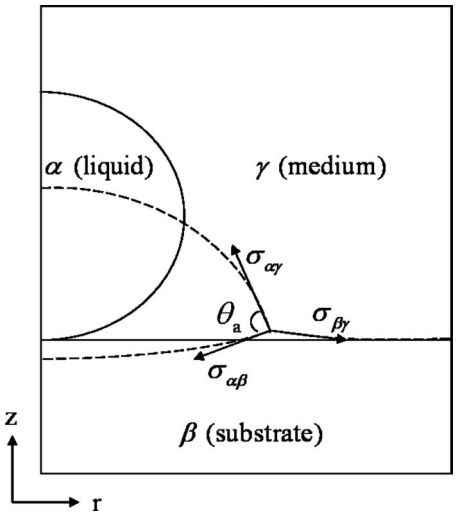

FIG. 1. The axisymmetric model where each phase α, β, and γ contains a fraction of substitutional elements A, B, and C. The governing equations are expressed in cylindrical coordinates (r,z). The angle θ_a is defined as the apparent contact angle and the σ's are interfacial energies. The triple junction is not assumed or forced to remain at the initial substrate height although it stays there during the early stage of spreading.

$$\begin{aligned} G_m = {} & [1 - P(\phi_\alpha) - P(\phi_\beta)] G_m^\gamma + P(\phi_\alpha) G_m^\alpha + P(\phi_\beta) G_m^\beta \\ & + W_{\alpha\beta} \phi_\alpha^2 \phi_\beta^2 + W_{\alpha\gamma} \phi_\alpha^2 (1 - \phi_\alpha - \phi_\beta)^2 \\ & + W_{\beta\gamma} \phi_\beta^2 (1 - \phi_\alpha - \phi_\beta)^2 + W_{\alpha\beta\gamma} \phi_\alpha^2 \phi_\beta^2 (1 - \phi_\alpha - \phi_\beta)^2, \end{aligned} \tag{2}$$

with the smoothed step function $P(\phi_i) = \phi_i^3 (10 - 15\phi_i + 6\phi_i^2)$, the same as in conventional phase-field formulations [18,32].

Since in the systems of study here do not have miscibility gap, i.e., are not prone to demixing or spinodal decomposition, the gradient terms in $x_{A,B,C}$ are not important and will not influence the results even if they are included. Similar approaches have been done by Folch and Plapp [33] in their ternary model that is applied to quantitative simulations of solidification.

For simplicity, we assume an ideal solution for $G_m^{\alpha,\beta,\gamma}$. For a ternary system we can then write the molar Gibbs energy as

$$\begin{aligned} G_m^i = {} & x_A {}^o G_A^i + x_B {}^o G_B^i + (1 - x_A - x_B) {}^o G_C^i + RT[x_A \ln x_A \\ & + x_B \ln x_B + (1 - x_A - x_B) \ln(1 - x_A - x_B)], \quad i = \alpha, \beta, \gamma \end{aligned} \tag{3}$$

where, for example, ${}^o G_A^\alpha$ is the molar Gibbs energy of an A lattice in the α phase without B and C atoms.

Considering an isothermal, viscous, and incompressible system, the governing equations are the following:

(i) convective concentration equations,

$$\frac{1}{V_m} \left(\frac{\partial x_A}{\partial t} + u \cdot \nabla x_A \right) = - \nabla \cdot J_A,$$

$$\frac{1}{V_m}\left(\frac{\partial x_B}{\partial t}+u\cdot\nabla x_B\right)=-\nabla\cdot J_B, \tag{4}$$

with natural boundary conditions $\mathbf{n}\cdot J_A=0$ and $\mathbf{n}\cdot J_B=0$;

(ii) convective Allen-Cahn equations for the phase-field variables which are nonconservative,

$$\frac{\partial\phi_\alpha}{\partial t}+u\cdot\nabla\phi_\alpha=-M_{\phi_\alpha}\frac{\delta G}{\delta\phi_\alpha},$$

$$\frac{\partial\phi_\beta}{\partial t}+u\cdot\nabla\phi_\beta=-M_{\phi_\beta}\frac{\delta G}{\delta\phi_\beta}, \tag{5}$$

where M_{ϕ_α} and M_{ϕ_β} are the kinetic mobilities and with natural boundary conditions $\mathbf{n}\cdot\nabla\phi_\alpha=0$ and $\mathbf{n}\cdot\nabla\phi_\beta=0$; and

(iii) and the Navier-Stokes equations with added surface tension and gravitational forces,

$$\rho(\phi)\left(\frac{\partial u}{\partial t}+u\cdot\nabla u\right)=-\nabla p+\nabla\cdot\mu(\phi)(\nabla u+\nabla u^T)-\sum_{i=\alpha,\beta,\gamma}\phi_i\nabla\left(\frac{\delta G}{\delta\phi_i}\right)+\rho(\phi)\mathbf{g},\nabla\cdot\mathbf{u}=0. \tag{6}$$

For the surface tension forcing, we follow the derivation of Jacqmin [34] (see the Appendix A).

The diffusion flux of solutes J_A and J_B are given by the Onsager linear law of irreversible thermodynamics,

$$J_A=-L_{AA}\nabla\left(\frac{\delta G}{\delta x_A}\right)-L_{AB}\nabla\left(\frac{\delta G}{\delta x_B}\right),$$

$$J_B=-L_{AB}\nabla\left(\frac{\delta G}{\delta x_A}\right)-L_{BB}\nabla\left(\frac{\delta G}{\delta x_B}\right), \tag{7}$$

where the chemical mobilities are given by

$$L_{AA}=(1-x_A)^2x_AM_A(\phi)+x_A^2x_BM_B(\phi)+x_A^2(1-x_A-x_B)M_C(\phi),$$

$$L_{BB}=x_B^2x_AM_A(\phi)+(1-x_B)^2x_BM_B(\phi)+x_B^2(1-x_A-x_B)M_C(\phi),$$

$$L_{AB}=-(1-x_A)x_Ax_BM_A(\phi)-x_Ax_B(1-x_B)M_B(\phi)+x_A(1-x_A-x_B)x_BM_C(\phi), \tag{8}$$

and

$$\frac{\delta G}{\delta x_j}=\frac{1}{V_m}\frac{\partial G_m}{\partial x_j},\quad j=A,B. \tag{9}$$

$M_A(\phi)$, $M_B(\phi)$, and $M_C(\phi)$ are the atomic mobilities of A, B, and C, respectively.

The phase-field equation for the α phase becomes

$$\begin{aligned}\frac{\partial\phi_\alpha}{\partial t}+u\cdot\nabla\phi_\alpha=-M_{\phi_\alpha}\Bigg[&\frac{1}{V_m}\{P'(\phi_\alpha)[x_A({}^oG_A^\alpha-{}^oG_A^\gamma)+x_B({}^oG_B^\alpha-{}^oG_B^\gamma)+(1-x_A-x_B)\\&\times({}^oG_C^\alpha-{}^oG_C^\gamma)]+2W_{\alpha\beta}\phi_\alpha\phi_\beta^2+2W_{\alpha\gamma}\phi_\alpha(1-\phi_\alpha-\phi_\beta)(1-2\phi_\alpha-\phi_\beta)\\&-2W_{\beta\gamma}\phi_\beta^2(1-\phi_\alpha-\phi_\beta)+2W_{\alpha\beta\gamma}\phi_\alpha\phi_\beta^2(1-\phi_\alpha-\phi_\beta)(1-2\phi_\alpha-\phi_\beta)\}\\&-\epsilon_\alpha^2\nabla^2\phi_\alpha+\epsilon_\gamma^2\nabla^2(1-\phi_\alpha-\phi_\beta)\Bigg],\end{aligned} \tag{10}$$

Note that the kinetic parameter M_{ϕ_i} is related to the normal grain-boundary mobility M [35] as $M_\phi=\frac{0.235M}{L_c}$, where L_c is the characteristic length.

Similar to Cahn and Hilliard [36], one may derive the following equations for the interfacial energy and thickness, respectively:

$$\sigma=\int_0^1\epsilon\left\{\frac{2}{V_m}\left[(G_m-G_m^{\text{phase}})-\sum_{j=1}^{n-1}\left.\frac{\partial G_m}{\partial x_j}\right|_{\text{phase}}(x_j-x_j|_{\text{phase}})\right]\right\}^{1/2}d\phi, \tag{11}$$

and

$$\delta^2=\epsilon^2\frac{V_m}{2}\left[(G_m-G_m^{\text{phase}})-\sum_{j=1}^{n-1}\left.\frac{\partial G_m}{\partial x_j}\right|_{\text{phase}}(x_j-x_j|_{\text{phase}})\right]_{\max}^{-1}. \tag{12}$$

In the practical calculation, the "phase" stands for α when evaluating $\sigma_{\alpha\beta}$ and $\delta_{\alpha\beta}$ and γ when evaluating $\sigma_{\alpha\gamma}$, $\delta_{\alpha\gamma}$, $\sigma_{\beta\gamma}$, and $\delta_{\beta\gamma}$.

Now, define characteristic scales

$$\tilde{u}=\frac{u}{U_c},\quad \tilde{x}=\frac{x}{L_c},\quad \tilde{t}=\frac{t}{T_c}=\frac{tL_c}{U_c},\quad \tilde{p}=\frac{pL_c}{\mu_cU_c}, \tag{13}$$

and introduce characteristic surface tension σ_c and interface thickness δ_c. Also define dimensionless parameters,

$$\eta_A^\alpha=\frac{\delta_c({}^oG_A^\alpha-{}^oG_A^\gamma)}{\sigma_cV_m},\quad \eta_B^\alpha=\frac{\delta_c({}^oG_B^\alpha-{}^oG_B^\gamma)}{\sigma_cV_m},$$

$$\eta_C^\alpha=\frac{\delta_c({}^oG_C^\alpha-{}^oG_C^\gamma)}{\sigma_cV_m},\quad \eta_A^\beta=\frac{\delta_c({}^oG_A^\beta-{}^oG_A^\gamma)}{\sigma_cV_m},$$

$$\eta_B^\beta=\frac{\delta_c({}^oG_B^\beta-{}^oG_B^\gamma)}{\sigma_cV_m},\quad \eta_C^\beta=\frac{\delta_c({}^oG_C^\beta-{}^oG_C^\gamma)}{\sigma_cV_m},$$

$$\eta_A^\gamma = \frac{\delta_c {}^oG_A^\gamma}{\sigma_c V_m}, \quad \eta_B^\gamma = \frac{\delta_c {}^oG_B^\gamma}{\sigma_c V_m}, \quad \eta_C^\gamma = \frac{\delta_c {}^oG_C^\gamma}{\sigma_c V_m},$$

$$\tilde{W}_{\alpha\beta} = \frac{W_{\alpha\beta}\delta_c}{\sigma_c V_m}, \quad \tilde{W}_{\alpha\gamma} = \frac{W_{\alpha\gamma}\delta_c}{\sigma_c V_m}, \quad \tilde{W}_{\beta\gamma} = \frac{W_{\beta\gamma}\delta_c}{\sigma_c V_m},$$

$$\tilde{W} = \frac{W_{\alpha\beta\gamma}\delta_c}{\sigma_c V_m}, \quad \tilde{V} = \frac{\delta_c RT}{\sigma_c V_m},$$

$$\hat{\epsilon}_\alpha^2 = \frac{\epsilon_\alpha^2}{\delta_c \sigma_c}, \quad \hat{\epsilon}_\beta^2 = \frac{\epsilon_\beta^2}{\delta_c \sigma_c}, \quad \hat{\epsilon}_\gamma^2 = \frac{\epsilon_\gamma^2}{\delta_c \sigma_c},$$

$$\mathrm{Pe}_{\phi_\alpha} = \frac{U_c \delta_c}{M_{\phi_\alpha} \sigma_c L_c}, \quad \mathrm{Pe}_{\phi_\beta} = \frac{U_c \delta_c}{M_{\phi_\beta} \sigma_c L_c}, \quad \mathrm{Cn} = \frac{\delta_c}{L_c},$$

and dropping the tildes yields the nondimensional version of Eq. (10) as follows:

$$\frac{\partial \phi_\alpha}{\partial t} + u \cdot \nabla \phi_\alpha = -\frac{1}{\mathrm{Pe}_{\phi_\alpha}}[\{P'(\phi_\alpha)[x_A \eta_A^\alpha + x_B \eta_B^\alpha + (1 - x_A - x_B)\eta_C^\alpha] + 2W_{\alpha\beta}\phi_\alpha\phi_\beta^2 + 2W_{\alpha\gamma}\phi_\alpha(1 - \phi_\alpha - \phi_\beta)(1 - 2\phi_\alpha - \phi_\beta)$$
$$- 2W_{\beta\gamma}\phi_\beta^2(1 - \phi_\alpha - \phi_\beta) + 2W\phi_\alpha\phi_\beta^2(1 - \phi_\alpha - \phi_\beta)(1 - 2\phi_\alpha - \phi_\beta)\} - \hat{\epsilon}_\alpha^2 \mathrm{Cn}^2 \nabla^2 \phi_\alpha + \hat{\epsilon}_\gamma^2 \mathrm{Cn}^2 \nabla^2 (1 - \phi_\alpha - \phi_\beta)]. \tag{14}$$

Similarly,

$$\frac{\partial \phi_\beta}{\partial t} + u \cdot \nabla \phi_\beta = -\frac{1}{\mathrm{Pe}_{\phi_\beta}}[\{P'(\phi_\beta)[x_A \eta_A^\beta + x_B \eta_B^\beta + (1 - x_A - x_B)\eta_C^\beta] + 2W_{\alpha\beta}\phi_\alpha^2\phi_\beta - 2W_{\alpha\gamma}\phi_\alpha^2(1 - \phi_\alpha - \phi_\beta) + 2W_{\beta\gamma}\phi_\beta(1 - \phi_\alpha - \phi_\beta)$$
$$\times(1 - \phi_\alpha - 2\phi_\beta) + 2W\phi_\alpha^2\phi_\beta(1 - \phi_\alpha - \phi_\beta)(1 - \phi_\alpha - 2\phi_\beta)\} - \hat{\epsilon}_\beta^2 \mathrm{Cn}^2 \nabla^2 \phi_\beta + \hat{\epsilon}_\gamma^2 \mathrm{Cn}^2 \nabla^2 (1 - \phi_\alpha - \phi_\beta)]. \tag{15}$$

For the concentration equations,

$$\frac{\partial x_A}{\partial t} + u \cdot \nabla x_A = \nabla \cdot \left\{ [(1 - x_A)^2 x_B M_A(\phi) + x_A^2 x_B M_B(\phi) + x_A^2 (1 - x_A - x_B) M_C(\phi)] \left(\frac{\partial^2 G_m}{\partial x_A^2} \nabla x_A + \frac{\partial^2 G_m}{\partial x_A \partial x_B} \nabla x_B + \frac{\partial^2 G_m}{\partial x_A \partial \phi_\alpha} \nabla \phi_\alpha \right.\right.$$
$$\left. + \frac{\partial^2 G_m}{\partial x_A \partial \phi_\beta} \nabla \phi_\beta \right) + \frac{1}{V_m^2}[-(1 - x_A) x_A x_B M_A - x_A x_B (1 - x_B) M_B + x_A (1 - x_A - x_B) x_B M_C] \left(\frac{\partial^2 G_m}{\partial x_B^2} \nabla x_B \right.$$
$$\left.\left. + \frac{\partial^2 G_m}{\partial x_B \partial x_A} \nabla x_A + \frac{\partial^2 G_m}{\partial x_B \partial \phi_\alpha} \nabla \phi_\alpha + \frac{\partial^2 G_m}{\partial x_B \partial \phi_\beta} \nabla \phi_\beta \right) \right\}. \tag{16}$$

Define dimensionless parameters,

$$\mathrm{Pe} = \frac{U_c L_c}{M_c RT}, \quad \tilde{M}_A(\phi) = \frac{M_A(\phi)}{M_c}, \quad \tilde{M}_B(\phi) = \frac{M_B(\phi)}{M_c}, \quad \tilde{M}_C(\phi) = \frac{M_C(\phi)}{M_c}, \quad \hat{\eta}_A^\alpha = \frac{{}^oG_A^\alpha - {}^oG_A^\gamma}{RT},$$

$$\hat{\eta}_B^\alpha = \frac{{}^oG_B^\alpha - {}^oG_B^\gamma}{RT}, \quad \hat{\eta}_C^\alpha = \frac{{}^oG_C^\alpha - {}^oG_C^\gamma}{RT}, \quad \hat{\eta}_A^\beta = \frac{{}^oG_A^\beta - {}^oG_A^\gamma}{RT}, \quad \hat{\eta}_B^\beta = \frac{{}^oG_B^\beta - {}^oG_B^\gamma}{RT}, \quad \hat{\eta}_C^\beta = \frac{{}^oG_C^\beta - {}^oG_C^\lambda}{RT},$$

and dropping the tildes,

$$\frac{\partial x_A}{\partial t} + u \cdot \nabla x_A = \frac{1}{\mathrm{Pe}} \nabla \cdot \left\{ [(1 - x_A)^2 x_B M_A(\phi) + x_A^2 x_B M_B(\phi) + x_A^2 (1 - x_A - x_B) M_C(\phi)] \left(\frac{1 - x_B}{x_A (1 - x_A - x_B)} \nabla x_A + \frac{1}{1 - x_A - x_B} \nabla x_B \right.\right.$$
$$\left. + P'(\phi_\alpha)(\hat{\eta}_A^\alpha - \hat{\eta}_C^\alpha) \nabla \phi_\alpha + P'(\phi_\beta)(\hat{\eta}_A^\beta - \hat{\eta}_C^\beta) \nabla \phi_\beta \right) + [-(1 - x_A) x_A x_B M_A(\phi) - x_A x_B (1 - x_B) M_B(\phi)$$
$$+ x_A (1 - x_A - x_B) x_B M_C(\phi)] \left(\frac{1}{1 - x_A - x_B} \nabla x_A + \frac{1 - x_A}{x_B (1 - x_A - x_B)} \nabla x_B + P'(\phi_\alpha)(\hat{\eta}_B^\alpha - \hat{\eta}_C^\alpha) \nabla \phi_\alpha \right.$$
$$\left.\left. + P'(\phi_\beta)(\hat{\eta}_B^\beta - \hat{\eta}_C^\beta) \nabla \phi_\beta \right) \right\}. \tag{17}$$

Similarly,

$$\frac{\partial x_B}{\partial t} + u \cdot \nabla x_B = \frac{1}{\mathrm{Pe}} \nabla \cdot \left\{ [-(1-x_A)x_A x_B M_A(\phi) - x_A x_B (1-x_B) M_B(\phi) + x_A x_B (1-x_A-x_B) M_C(\phi)] \right.$$
$$\times \left(\frac{1-x_B}{x_A(1-x_A-x_B)} \nabla x_A + \frac{1}{1-x_A-x_B} \nabla x_B + P'(\phi_\alpha)(\hat{\eta}_A^\alpha - \hat{\eta}_C^\alpha) \nabla \phi_\alpha + P'(\phi_\beta)(\hat{\eta}_A^\beta - \hat{\eta}_C^\beta) \nabla \phi_\beta \right)$$
$$+ [x_A x_B^2 M_A + x_B(1-x_B)^2 M_B + x_B^2(1-x_A-x_B) M_C]$$
$$\left. \times \left[\frac{1}{1-x_A-x_B} \nabla x_A + \frac{1-x_A}{x_B(1-x_A-x_B)} \nabla x_B + P'(\phi_\alpha)(\hat{\eta}_B^\alpha - \hat{\eta}_C^\alpha) \nabla \phi_\alpha + P'(\phi_\beta)(\hat{\eta}_B^\beta - \hat{\eta}_C^\beta) \nabla \phi_\beta \right] \right\}. \quad (18)$$

For the Navier-Stokes equations, we introduce characteristic scales and define dimensionless parameters,

$$\mathrm{Re} = \frac{\rho_c U_c L_c}{\mu_c}, \quad \mathrm{Ca} = \frac{\mu_c U_c}{\sigma_c}, \quad \mathrm{Bo} = \frac{\rho_c g L_c^2}{\sigma_c}.$$

Then,

$$\mathrm{Re}\ \rho(\phi)\left(\frac{\partial u}{\partial t} + u \cdot \nabla u \right) = -\nabla p + \nabla \cdot \mu(\phi)(\nabla u + \nabla u^T)$$
$$- \frac{1}{\mathrm{Ca}} \frac{1}{\mathrm{Cn}} \sum_{i=\alpha,\beta,\gamma} \phi_i \nabla \left(\frac{\delta G}{\delta \phi_i} \right)$$
$$+ \frac{\mathrm{Bo}}{\mathrm{Ca}} \rho(\phi) \mathbf{g}. \quad (19)$$

The Reynolds number is the ratio between the inertial and viscous forces. The capillary number gives the ratio between the viscous and surface tension forces, while the Bond number is the ratio between the gravitational and surface tension forces. We have added the gravity forces in the formulation but they will be neglected in the succeeding numerical simulations.

We model the mobilities (M_j's), density (ρ), and viscosity (μ) functions by

$$M_j(\phi) = M_j^\alpha \phi_\alpha + M_j^\beta \phi_\beta + M_j^\gamma (1 - \phi_\alpha - \phi_\beta), \quad j = A, B, C,$$

$$\rho(\phi) = \rho_\alpha \phi_\alpha + \rho_\beta \phi_\beta + \rho_\gamma (1 - \phi_\alpha - \phi_\beta),$$

$$\mu(\phi) = \begin{cases} \mu_\alpha \phi_\alpha + \mu_\gamma (1 - \phi_\alpha - \phi_\beta) \text{ if } \phi_\beta \le 0.8 \\ \mu_\gamma + 0.5(\mu_\beta - \mu_\gamma) \left[1 + \tanh\left(\frac{2\pi(\phi_\beta - 0.8)}{0.6} \right) \right], \text{ else.} \end{cases} \quad (20)$$

The viscosity function given allows us to model solid phases with high viscosity.

III. NUMERICAL TREATMENT

The numerical simulations were carried out using the FemLego [37], an open source symbolic tool to solve partial differential equations with the adaptive finite element method. We consider an axisymmetric model where the rotational symmetry is around the vertical axis (see Fig. 1).

The boundary conditions given for the composition and phase-field equations are natural boundary conditions. So,

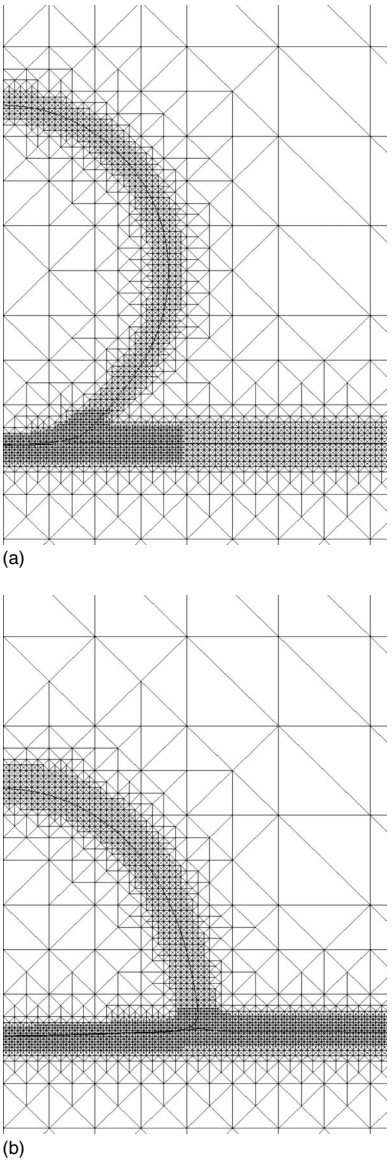

FIG. 2. The adaptive mesh at two different times with a superimposed contour plot of the phase-field variables.

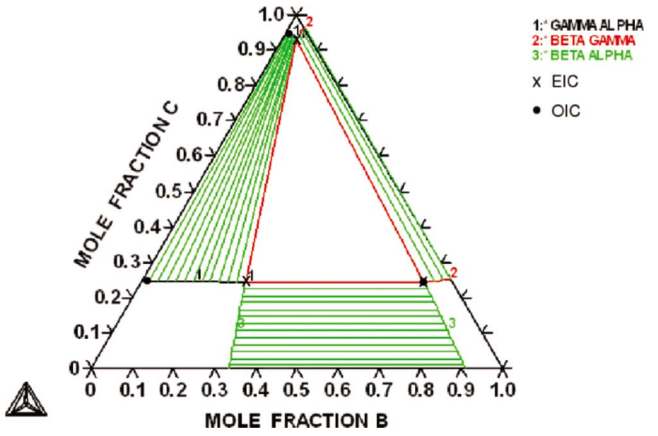

FIG. 3. (Color online) Calculated phase diagram of an arbitrary $A-B-C$ system at 1527 °C. The three crosses and dots represent the initial composition in the α, β, and γ phases used for the EIC and OIC cases, respectively.

taking the variational formulation of the partial differential equations and applying integration by parts, the boundary integrals will vanish. Both the composition and phase-field equations are discretized in space using piecewise linear functions. The resulting linear systems are solved using the generalized minimum residual method. The Navier-Stokes equations are solved using a projection method by Guermond and Quartapelle [38] with an added pressure stabilization term. The Navier-Stokes equations are also discretized in space using piecewise linear functions and the linear systems are solved using the conjugate gradient method.

Since the model requires the interface to be resolved, the use of adaptivity is essential. An *ad hoc* error criterion is used to ensure mesh resolution along the vicinity of the interface (see Fig. 2). The mesh adaptivity is implemented as follows: at each mesh refinement step, an element K is marked for refinement if the element size $h > h_{\min}$ (the minimum h allowed), and does not satisfy the following error criterion:

$$\|H[a - |\phi_i(x,t) - 0.5|]\|_{L^1(K)} \leq \mathrm{TOL}, \tag{21}$$

where $H(\cdot)$ is the Heaviside step function, a is a constant (here we used $a=0.45$), and TOL is a given tolerance. If an element satisfies the error criterion, it is marked for derefinement unless it is an original element. At the next refinement step, elements containing hanging nodes are marked for refinement. The refinement or derefinement stops if and only if no element is marked for refinement or derefinement.

IV. INPUT PARAMETERS

A. Phase diagram

The model presented allows for arbitrary phase diagrams, such as the one shown in Fig. 3, which was generated using Thermo-Calc software [44]. The phase diagram is idealized with the molar Gibbs energy (${}^oG_j^i$) of an i lattice in a j phase without the other atoms, to be of the same order of magnitude as $R*T$ (gas constant R, temperature T). The phase diagram is also presented in a nondimensional form and for generality does not represent one particular system or material. This system has a very low component of both A and B in the γ phase (medium) mimicking a void. The α phase (spreading liquid) contains a higher amount of A than B and the β phase (substrate) contains mostly B. Although the substrate is usually of pure material and the medium is vapor in many dissolutive systems, we defer a detailed comparison with such systems in succeeding work. Our aim is to present a diffuse-interface model that can be used to analyze reactive wetting as a process controlled by diffusion and fluid flow.

The phase diagram in Fig. 3 shows the equilibrium composition in the α, β, and γ phase. In this paper, we examine two cases for the initial composition, first, using the equilibrium composition as an initial condition for the concentration variables x_A and x_B, and second, an off-equilibrium initial composition, i.e., represented by dots in Fig. 3. More specifically,

EIC (equilibrium initial composition):

composition of A: [0.5,0.07,0.03],

composition of B: [0.26,0.69,0.04],

OIC (off-equilibrium initial composition):

composition of A: [0.73,0.07,0.03],

composition of B: [0.03,0.69,0.02].

The entries in the A composition's (or B's) correspond to the mole fraction of A (or B) in the α, β, and γ phases, respectively.

B. Surface energies

Another set of input parameters are the surface energies and interface thicknesses. Here, we examine three cases. See Table I for the input parameters and Table III for the corresponding interfacial energies using Eq. (11) (see Appendix B for the dimensionless expressions).

TABLE I. Surface energy input parameters.

	$W_{\alpha\beta}$	$W_{\alpha\gamma}$	$W_{\beta\gamma}$	$\hat{\epsilon}_h^2 a$	$\hat{\epsilon}_\beta^2$	$\hat{\epsilon}_\gamma^2$
SE1	6.890	8.559	17.912	0.041	2.401	2.520
SE2	6.890	8.559	13.906	0.542	1.900	2.019
SE3	6.890	8.559	8.438	1.225	1.217	1.335

TABLE II. Base set of parameters.

Ca=1.0	$\hat{\eta}_A^\alpha=-2.673$	$\eta_A^\alpha=-0.571$	$\eta_A^\gamma=0.286$	$M_B^\alpha=1.0$	$\rho_\alpha=10$
Re=1.0	$\hat{\eta}_B^\alpha=-2.005$	$\eta_B^\alpha=-0.429$	$\eta_B^\gamma=0.286$	$M_B^\beta=0.001$	$\rho_\beta=10$
Pe=10^4	$\hat{\eta}_C^\alpha=1.336$	$\eta_C^\alpha=0.286$	$\eta_C^\gamma=-0.143$	$M_B^\gamma=1.0$	$\rho_\gamma=1$
$\mathrm{Pe}_{\phi_\alpha}=100$	$\hat{\eta}_A^\beta=-0.668$	$\eta_A^\beta=-0.143$	$M_A^\alpha=1.0$	$M_C^\alpha=1.0$	$\mu_\alpha=1$
$\mathrm{Pe}_{\phi_\beta}=100$	$\hat{\eta}_B^\beta=-3.007$	$\eta_B^\beta=-0.643$	$M_A^\beta=0.001$	$M_C^\beta=0.001$	$\mu_\beta=10^5$
$W=600$	$\hat{\eta}_C^\beta=1.336$	$\eta_C^\beta=0.286$	$M_A^\gamma=1.0$	$M_C^\gamma=1.0$	$\mu_\gamma=1$

C. Choice of other parameters

The input Ca number is the nominal capillary number $\mathrm{Ca}=(\mu_c U_c)/(\sigma_c)$, where U_c is the characteristic velocity. However, there is also an actual or effective capillary number $\mathrm{Ca}^*=(\mu_c U)/(\sigma_c)$, where U is the actual wetting speed. Now, if we set Ca=1, this means $U_c=\sigma_c/\mu_c$ and the actual Ca^* becomes U/U_c, which is the dimensionless wetting speed. Inertial effects are assumed low, so Re=1.0. The η's correspond to the phase diagram selected (see Table II). Following [18], we choose the parameter W to be sufficiently large in order to properly calculate each of the i/j-surface energies with W_{ij} by locally suppressing the foreign third phase. The mobility in the β phase (substrate) is much smaller than in the α (liquid) and γ (medium) phases. The density of the substrate is the same as the spreading liquid and both are ten times greater than the medium. Moreover, the viscosity of the substrate is 10^5 times higher than the liquid and the medium.

We note here that the parameters in Tables I and II are not chosen randomly but represent reasonable physical situations. In general, we consider capillary-driven laminar flows. For example, the Reynolds number Re being the ratio between the inertial and viscous forces, is assumed to be of order unity or less, typical in most reactive wetting systems. The capillary number provides the ratio between the viscous and capillary forces and is also assumed to be of order unity or less. Two sets of diffusion parameters are used and they relate the ratio between the convective and diffusive mass transport.

V. RESULTS AND DISCUSSION

We observed two stages in the wetting process. First, the convection-dominated stage where rapid spreading occurs and the drop approaches a quasi-steady state, and second, the diffusion-dominated stage where diffusion-controlled mechanisms are observed such as depression of the substrate-liquid interface, elevation of the contact line region, and possibly shrinkage or expansion of the spreading liquid depending on the parameters chosen. Similarly, the experimental work of Shen *et al.* [39] on high-temperature reactive wetting identified three stages in the wetting process: a fast spreading stage, followed by a transition stage, then a long and progressive spreading stage.

A. Convection-dominated stage

This stage is manifested by rapid spreading. Figure 4 shows contour plots (level 0.5) of the phase-field variables with EIC for three cases: (a) SE1, (b) SE2, (c) SE3, at times $t=0$, 8, 15, and 100 (marked 0,1,2,3), respectively. In Fig. 4(a), the liquid drop initially starts with a spherical shape (marked 0). The drop rapidly spreads and at time $t=1$, the velocity profile is given in Fig. 5(a) showing a vortex with a center along the interface. The figure also shows zero velocity in the substrate, which was modeled by high viscosity. Then at $t=8$ [marked 1 in Fig. 4(a)], the drop makes an apparent contact angle of $\theta_a=93°$ with drop base radius $R=1.0$. Apparent contact angles were measured with an image processing software IMAGEJ [45] using contour plots (level 0.5) of the phase-field variables in which tangent lines are drawn at the "macroscopic foot" of the spreading liquid (with the tangent lines coinciding with the corresponding point where the contour lines start to separate neglecting the inner structure of the contact line region in the measurement). At time $t=15$ (marked 2), the drop further spreads and $\theta_a=68°$ with $R=1.35$. Then at $t=100$, the drop makes an apparent contact angle $\theta_a=30°$ and $R=1.86$. The velocity profile is given in Fig. 5(b) with a maximum velocity of 0.0015, much slower compared to a maximum velocity of 0.1135 at $t=1$. The change of the apparent contact angle with respect to time is plotted in Fig. 6 suggesting that the wetting is fast where the apparent contact angle decreases rapidly and then slows down upon reaching a quasisteady state. This is similar to the rapid isothermal spreading of a drop in contact with a substrate observed experimentally by Voitovich *et al.* [40].

TABLE III. Comparison between the quasisteady equilibrium contact angle θ_m using Young's equation and the measured apparent contact angle θ_a at $t=100$.

	$\sigma_{\alpha\beta}$	$\sigma_{\alpha\gamma}$	$\sigma_{\beta\gamma}$	θ_m	θ_a
SE1	0.949	0.792	1.589	36°	30°
SE2	0.949	0.785	1.242	68°	58°
SE3	0.949	0.791	0.795	101°	98°

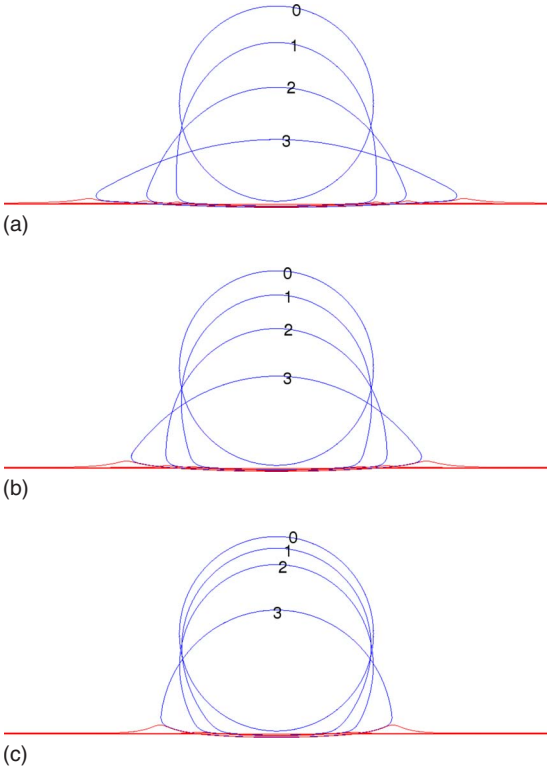

FIG. 4. (Color online) The contour plots (level 0.5) of the phase-field variables for the EIC case with (a) SE1, (b) SE2, and (c) SE3, at time $t=0,8,15,100$ (marked 0,1,2,3), respectively.

This case corresponds to $\sigma_{\alpha\beta}=0.949$, $\sigma_{\alpha\gamma}=0.792$, and $\sigma_{\beta\gamma}=1.589$ using Eq. (11) (see Table III). Using the Young's equation [41], $\sigma_{\alpha\gamma}\cos\theta_m=\sigma_{\beta\gamma}-\sigma_{\alpha\beta}$, we found that $\theta_m=36°$ compared to the measured apparent contact angle of $\theta_a=30°$ at $t=100$. With SE2, the corresponding quasisteady equilibrium contact angle using Young's equation is 68° while at $t=100$ [marked 3 in Fig. 4(b)], the measured apparent contact angle is 58°. The quasisteady contact angle for the case SE3 is 101° while at $t=100$ [marked 3 in Fig. 4(c)], the apparent contact angle is measured to be 98°. However, due to diffusion as manifested by the elevation of the contact line region, we expect that the equilibrium contact angle that θ_a will approach in the long term can be calculated using Neumann's construction [41], given by $\vec{\sigma}_{\alpha\beta}+\vec{\sigma}_{\alpha\gamma}+\vec{\sigma}_{\beta\gamma}=0$, which means that the horizontal and vertical components of the surface tension forces must sum up to zero. The long term equilibrium contact angles of 48°, 88°, and 126° for the three cases, SE1, SE2, and SE3, respectively, have been computed. We have observed a tendency for the apparent contact angles to increase in the diffusion-dominated stage but not simulated far enough to be able to check if the apparent contact angle reaches the long term equilibrium contact angles. There is also a possible shrinkage or expansion of the spreading liquid which in the long term, the liquid could disappear without even reaching the equilibrium contact angle given by the Neumann's construction.

With the OIC, very similar configurations in each SE1, SE2, and SE3 case until $t=100$ have been obtained. The evolution of the drop base radius with respect to time for the six cases (a combination of EIC and OIC with SE1, SE2, and SE3) is shown in Fig. 7. The drop spreads the farthest with SE1, followed by SE2, and the shortest base radius with SE3. We also observed that at an early stage, both EIC and OIC have the same base radius and then the OIC case starts to deviate and spreads longer in time.

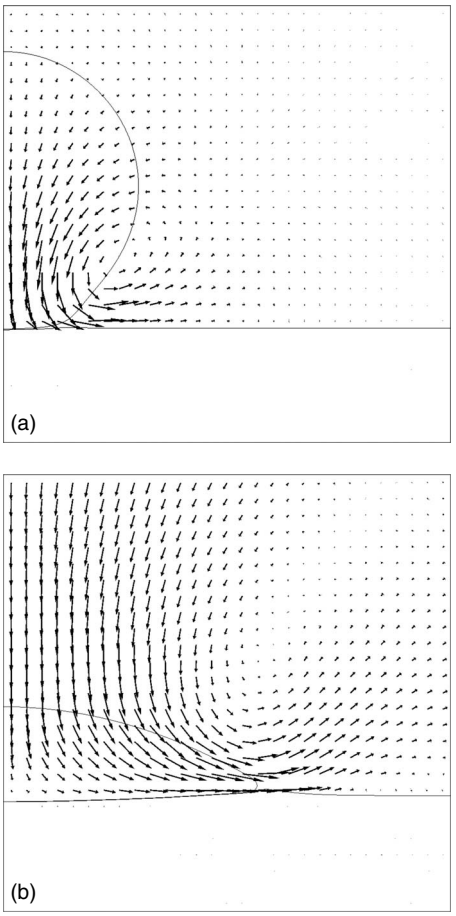

FIG. 5. Cutoff velocity profile of the EIC case with surface energy SE1 (a) at $t=1$ with $u_{\max}=0.1135$ and (b) at $t=100$ with $u_{\max}=0.0015$.

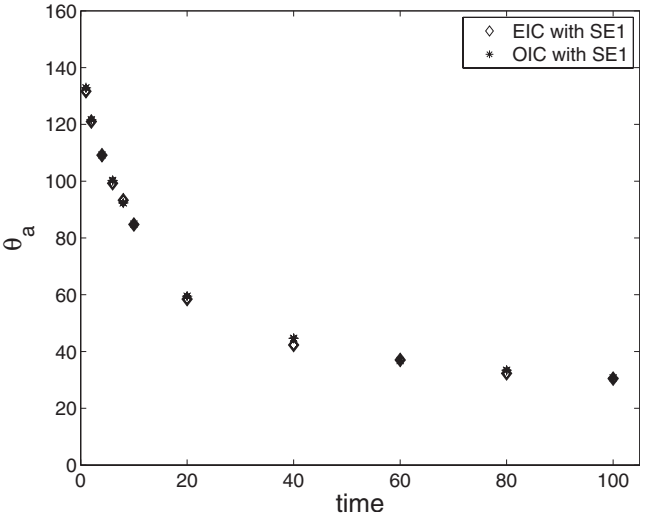

FIG. 6. Apparent contact angle vs dimensionless time for EIC and OIC with surface energy SE1.

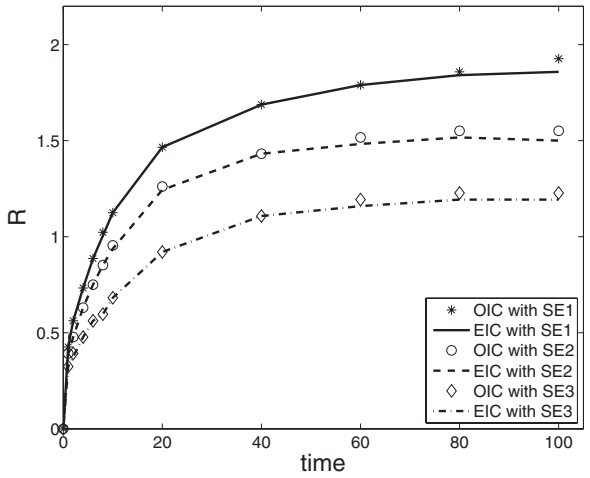

FIG. 7. The evolution of the drop base radius in time for EIC and OIC with surface energies SE1, SE2, SE3.

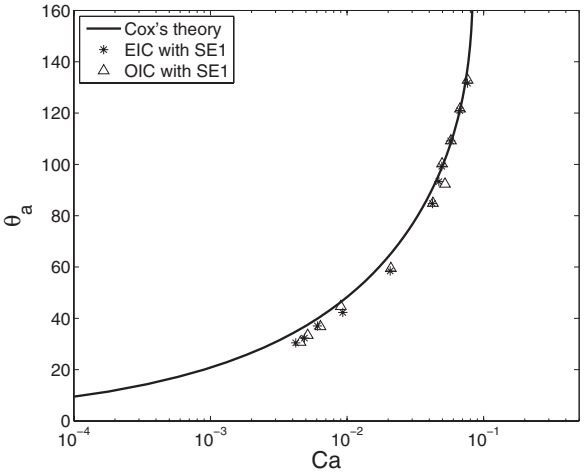

FIG. 8. Dynamics of the first stage of spreading with EIC and OIC compared to Cox's theory with viscosity ratio $\mu_\gamma/\mu_\alpha=1$ [42].

The dynamics of the early stage of wetting can be seen in Fig. 8. We observe a match between the EIC and OIC cases and Cox's theory [42] at a leading order with $\mu_\gamma/\mu_\alpha=1$ and a constant $\epsilon=10^{-2}$ (see Appendix C). The limited scatter that is present in Fig. 8 is attributed to uncertainties in determining the apparent contact angle. The figure also shows that whether the initial composition is at equilibrium or far from equilibrium, the dynamics of the wetting in the early stage is the same and obeys hydrodynamic laws. In comparison with the experimental work of Yin *et al.* [3] on the spreading of Bi-Sn on pure Bi susbtrates, their results also showed that the wetting behavior can be well described by hydrodynamic and molecular kinetic theories developed for inert systems. However, this is not the case for systems with higher diffusion parameters. Choosing, for example, $\mathrm{Pe}=10^3$, $\mathrm{Pe}_{\phi_\alpha}=5$, and $\mathrm{Pe}_{\phi_\beta}=5$, we observed faster spreading in both EIC and OIC than the predictions of Cox. This is not surprising since Cox's theory assumes no interdiffusion and the spreading is mainly governed by convective transport. A more obvious explanation is that diffusive transport significantly plays a role in every stage when high diffusion parameters are used.

B. Diffusion-dominated stage

Higher diffusion rates, i.e., $\mathrm{Pe}=10^3$, $\mathrm{Pe}_{\phi_\alpha}=5$, and $\mathrm{Pe}_{\phi_\beta}=5$ lead to shorter computational time whereas the effects induced by slow diffusion such as strong concentration gradients, depression of the substrate-liquid interface, elevation of the contact line region, and possible shrinkage or expansion of the spreading liquid lead to heavier computations.

Figure 9 shows concentration profiles of the A atoms for EIC [(a),(c),(e)] and OIC [(b),(d),(f)] with SE1 at times $t=0$, 10, and 175, respectively. Figure 9(a) shows the initial concentration of A for the EIC case and this has a maximum of 0.5 in the spreading liquid, 0.07 in the substrate, and 0.03 in the medium. For the OIC case, the maximum is 0.73 in the spreading liquid, 0.07 in the substrate, and 0.03 in the medium. At time $t=10$, both spread similarly [Figs. 9(c) and 9(d)] regardless of the initial concentration. Also in both cases, the concentration increases from 0.5 to 0.6 with the EIC and 0.73 to 0.84 with the OIC and appears at the top of the drop, where the curvature is strong due to the Gibbs-Thomson effect. Further spreading is observed in Figs. 9(e) and 9(f). This time, striking differences are observed. Apart from a strong gradient in concentration, the depression of the substrate liquid is noticeable, which is similar to previous experimental and numerical studies [2–4]. In both cases, the concentration evens out and the maximum concentration decreases as the top curvature decreases.

On the other hand, Fig. 10 shows the concentration profiles of the B atoms for the EIC [(a),(c),(e)] and OIC [(b),(d),(f)], both with SE1 at times $t=0$, 10, and 1/5, respectively. The maximum concentration is 0.69, which is in the substrate in all cases. With EIC [Fig. 10(a)], the concentration of B starts with 0.26 in the spreading liquid compared to a much smaller value of 0.03 in the OIC case [Fig. 10(b)]. In the succeeding Figs. 10(d) and 10(f), we see the transport of B atoms into the spreading liquid while there is no observable change in B concentration with EIC. This leads us to the conclusion that the transport of atoms across the interface changes the bulk energies causing the depression of the substrate-liquid interface.

VI. CONCLUSION

We have presented a multicomponent and multiphase model of reactive wetting. The governing equations were derived and nondimensionalized where typical dimensionless parameters were identified. Mesh adaptivity was implemented with an axisymmetric model.

Successful simulations of reactive wetting were performed revealing two stages in the process which are consistent with experimental studies [2,3,39]. First, the convection-dominated stage where rapid spreading occurs. A similar observation has been reported by Voitovich *et al.* [40] in their study of isothermal spreading of Cu-Cr alloys on carbon substrates. The dynamics of the rapid spreading for low diffusion parameters is shown to match a hydrodynamic theory by Cox for spreading liquids, which implies that the dynamic apparent contact angle is solely dependent on the capillary

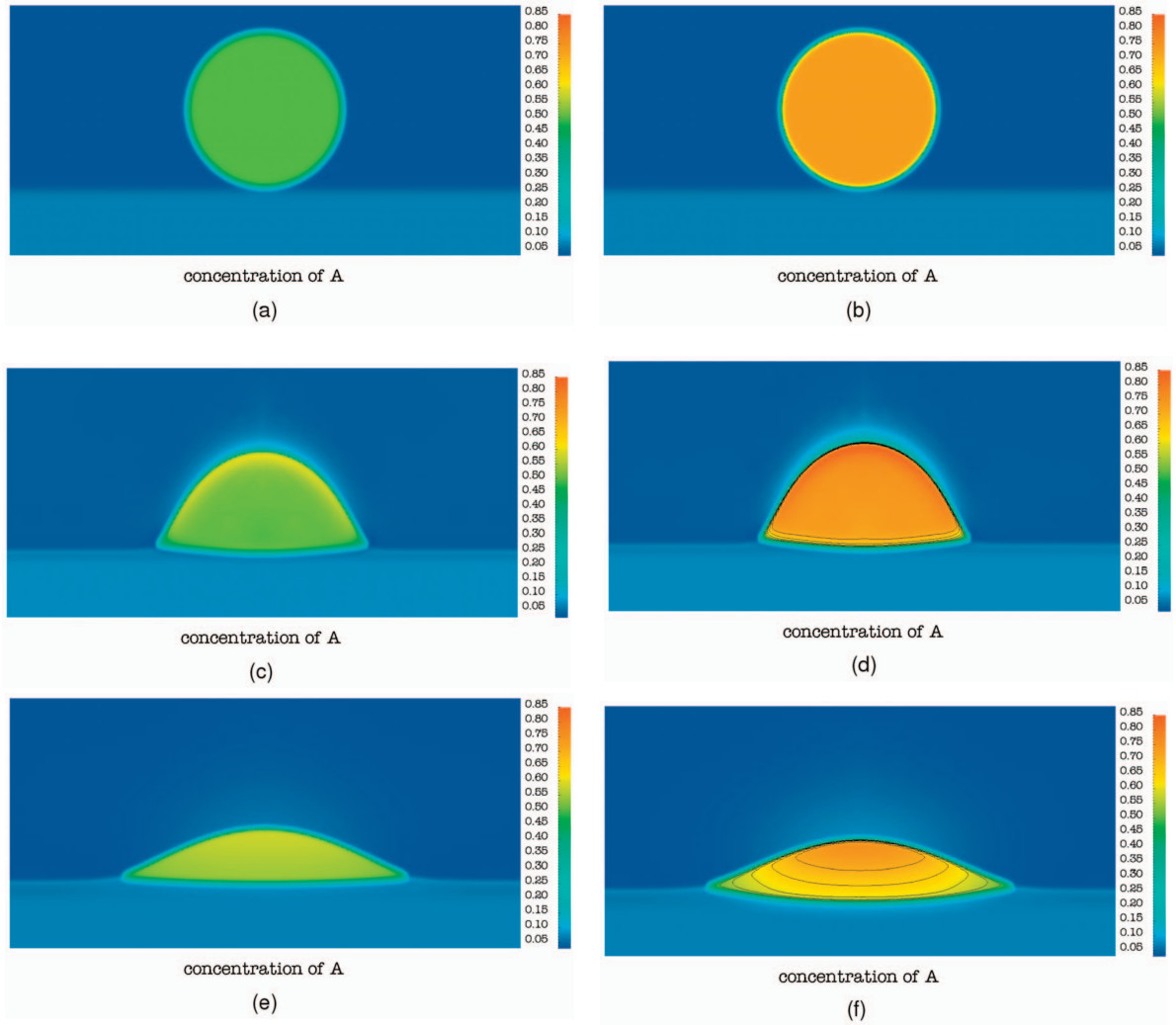

FIG. 9. (Color) Concentration profiles of the A atoms for EIC [(a),(c),(e)] and OIC [(b),(d),(f)] at times $t=0$, 10, and 175, respectively. Isolines are plotted in (d) and (f) with A isoconcentrates 0.50, 0.55, 0.60, 0.65, and 0.70 (out to inwards).

number, a result that is consistent with the experimental study of Yin *et al.* [3] on the spreading of Bi-Sn alloys on a pure Bi substrate.

Second, the diffusion-dominated stage where we observed depression of the substrate-liquid interface [Figs. 9(f) and 10(f)], which is qualitatively similar to the observations made in experiments of Bi-Sn spreading on pure Bi substrate [2,3] and to the molecular dynamics simulations of Ag spreading on Cu [4]. Another interesting observation is the elevation of the contact line region upon reaching an equilibrium state [seen more visibly in Fig. 4(c)], which is comparable to the experimental observations of Saiz *et al.* [7,8] in various systems.

In this paper we have analyzed realistic but still idealized systems. In the next step we shall apply the new approach to real systems including thermodynamic and kinetic information.

ACKNOWLEDGMENTS

The authors gratefully acknowledge the financial support from the Computational Phase Transformation program funded by the Swedish Foundation for Strategic Research (SSF). Part of the work (W.V. and G.A.) was carried out within the Linné Flow Centre.

APPENDIX A: SURFACE TENSION FORCING

Following the derivation by Jacqmin [34] for a binary system and by Zhou and Powell [43] for a ternary system, the Gibbs energy changes in time due to convection according to

$$\left.\frac{\partial G}{\partial t}\right|_{\text{conv}} = \int_{\Omega} \left[\left.\frac{\delta G}{\delta \phi_\alpha}\frac{\partial \phi_\alpha}{\partial t}\right|_{\text{conv}} + \left.\frac{\delta G}{\delta \phi_\beta}\frac{\partial \phi_\beta}{\partial t}\right|_{\text{conv}} \right] d\Omega.$$

Note that

$$\left.\frac{\partial \phi_\alpha}{\partial t}\right|_{\text{conv}} = -\nabla \cdot (u\phi_\alpha),$$

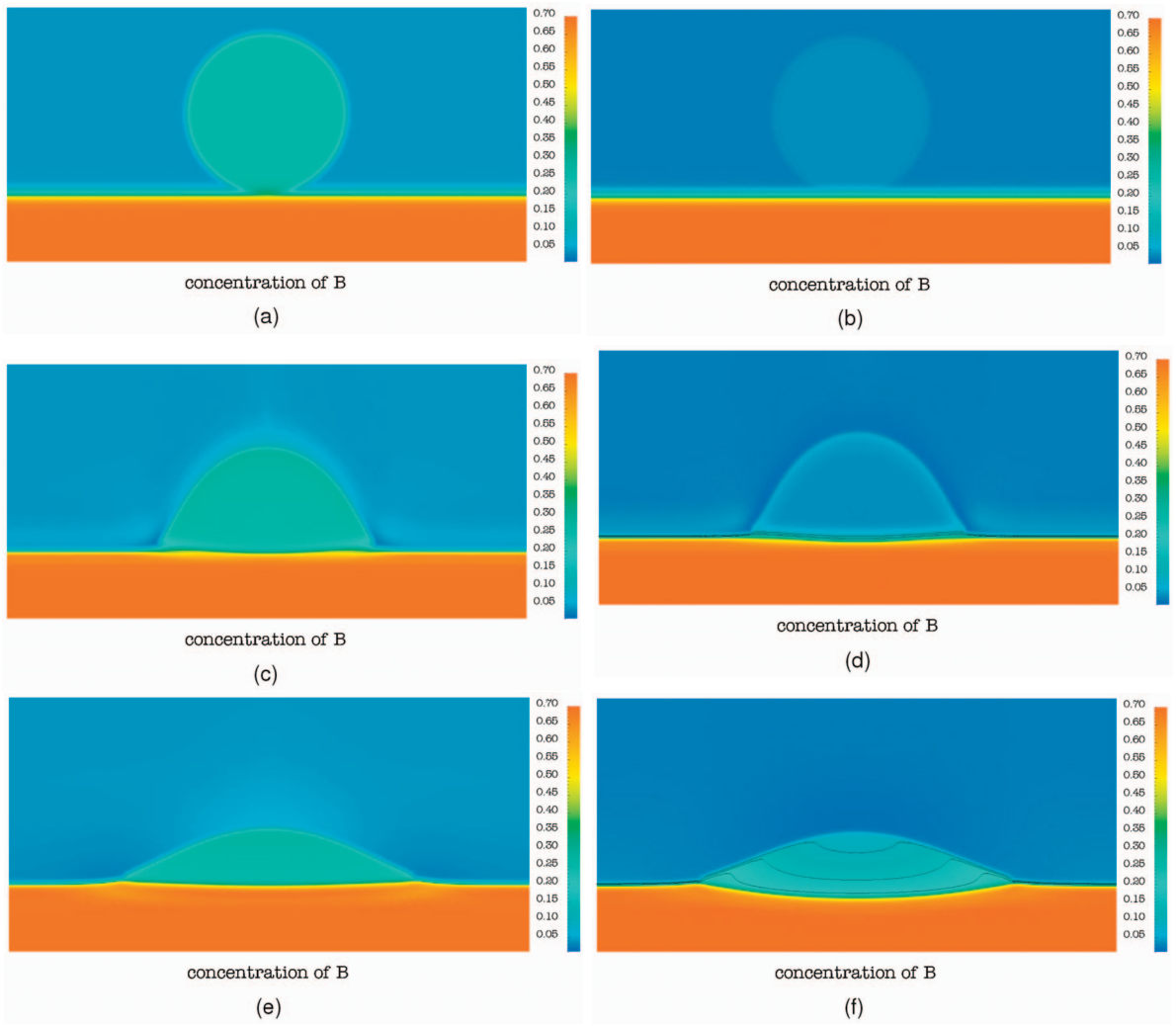

FIG. 10. (Color) Concentration profiles of the B atoms for EIC [(a),(c),(e)] and OIC [(b),(d),(f)] at times $t=0$, 10, and 175, respectively. Isolines are plotted in (d) and (f) with B isoconcentrates 0.10, 0.15, and 0.20 (top to bottom).

$$\left.\frac{\partial \phi_\beta}{\partial t}\right|_{\text{conv}} = -\nabla \cdot (u\phi_\beta).$$

Integration by parts combined with the divergence theorem yield

$$\left.\frac{\partial G}{\partial t}\right|_{\text{conv}} = -\int_\Omega \left[\frac{\delta G}{\delta \phi_\alpha}\nabla \cdot (u\phi_\alpha) + \frac{\delta G}{\delta \phi_\beta}\nabla \cdot (u\phi_\beta)\right] d\Omega$$

$$= -\int_{\partial\Omega} \mathbf{n} \cdot \left[\frac{\delta G}{\delta \phi_\alpha} u\phi_\alpha + \frac{\delta G}{\delta \phi_\beta} u\phi_\beta\right] dS.$$

The boundary integral vanishes due to boundary conditions. The rate of change of kinetic energy E due to surface tension forcing is always opposite to the change in free energy. Then,

$$-\left.\frac{\partial G}{\partial t}\right|_{\text{conv}} = \left.\frac{\partial E}{\partial t}\right|_{\text{kinetic}} = \int_\Omega uF d\Omega.$$

Thus the surface tension forcing is given by

$$F = -\sum_i \phi_i \nabla\left(\frac{\delta G}{\delta \phi_i}\right).$$

APPENDIX B: SURFACE TENSION AND INTERFACE THICKNESS

The interface thicknesses are defined as

$$\delta^2_{\alpha\beta} = \frac{(\epsilon^2_\alpha + \epsilon^2_\beta)V_m}{4}\left[(G_m - G^\alpha_m) - \left.\frac{\partial G_m}{\partial x_A}\right|_\alpha (x_A - x_A|_\alpha) - \left.\frac{\partial G_m}{\partial x_B}\right|_\alpha (x_B - x_B|_\alpha)\right]^{-1}_{\max},$$

$$\delta^2_{\alpha\gamma} = \frac{(\epsilon^2_\alpha + \epsilon^2_\gamma)V_m}{4}\left[(G_m - G^\gamma_m) - \left.\frac{\partial G_m}{\partial x_A}\right|_\gamma (x_A - x_A|_\gamma) - \left.\frac{\partial G_m}{\partial x_B}\right|_\gamma (x_B - x_B|_\gamma)\right]^{-1}_{\max},$$

$$\delta^2_{\beta\gamma} = \frac{(\epsilon^2_\beta + \epsilon^2_\gamma)V_m}{4}\left[G_m - G^\gamma_m - \left.\frac{\partial G_m}{\partial x_A}\right|_\gamma (x_A - x_A|_\gamma) - \left.\frac{\partial G_m}{\partial x_B}\right|_\gamma (x_B - x_B|_\gamma)\right]^{-1}_{\max}, \tag{B1}$$

and the surface tensions

$$\sigma_{\alpha\beta} = \int_0^1 \left(\frac{\epsilon^2_\alpha + \epsilon^2_\beta}{V_m}\left[(G_m - G^\alpha_m) - \left.\frac{\partial G_m}{\partial x_A}\right|_\alpha (x_A - x_A|_\alpha) - \left.\frac{\partial G_m}{\partial x_B}\right|_\alpha (x_B - x_B|_\alpha)\right]_{\phi_\gamma = 0}\right)^{1/2} d\phi,$$

$$\sigma_{\alpha\gamma} = \int_0^1 \left(\frac{\epsilon^2_\alpha + \epsilon^2_\gamma}{V_m}\left[(G_m - G^\gamma_m) - \left.\frac{\partial G_m}{\partial x_A}\right|_\gamma (x_A - x_A|_\gamma) - \left.\frac{\partial G_m}{\partial x_B}\right|_\gamma (x_B - x_B|_\gamma)\right]_{\phi_\beta = 0}\right)^{1/2} d\phi,$$

$$\sigma_{\beta\gamma} = \int_0^1 \left(\frac{\epsilon^2_\beta + \epsilon^2_\gamma}{V_m}\left[(G_m - G^\gamma_m) - \left.\frac{\partial G_m}{\partial x_A}\right|_\gamma (x_A - x_A|_\gamma) - \left.\frac{\partial G_m}{\partial x_B}\right|_\gamma (x_B - x_B|_\gamma)\right]_{\phi_\alpha = 0}\right)^{1/2} d\phi. \tag{B2}$$

Nondimensionalization takes the form

$$\tilde{\delta}^2_{\alpha\beta} = \frac{(\hat{\epsilon}^2_\alpha + \hat{\epsilon}^2_\beta)}{4}\left[\{[P(\phi_\alpha) - 1][x_A\eta^\alpha_A + x_B\eta^\alpha_B + (1 - x_A - x_B)\eta^\alpha_C] + P(\phi_\beta)[x_A\eta^\beta_A + x_B\eta^\beta_B + (1 - x_A - x_B)\eta^\beta_C] + \tilde{W}_{\alpha\beta}\phi^2_\alpha\phi^2_\beta\} - \left\{ (\eta^\gamma_A - \eta^\gamma_C) + \tilde{V}\ln\left(\frac{x_A}{1 - x_A - x_B}\right)_\alpha + P(\phi_\alpha)(\eta^\alpha_A - \eta^\alpha_C) + P(\phi_\beta)(\eta^\beta_A - \eta^\beta_C)\right\}(x_A - x_A|_\alpha) - \left\{ (\eta^\gamma_B - \eta^\gamma_C) + \tilde{V}\ln\left(\frac{x_B}{1 - x_A - x_B}\right)_\alpha + P(\phi_\alpha)(\eta^\alpha_B - \eta^\alpha_C) + P(\phi_\beta)(\eta^\beta_B - \eta^\beta_C)\right\}(x_B - x_B|_\alpha)\right]^{-1}_{\max}, \tag{B3}$$

and the surface tensions,

$$\tilde{\sigma}_{\alpha\beta} = \int_0^1 \left((\hat{\epsilon}^2_\alpha + \hat{\epsilon}^2_\beta)\left[\{[P(\phi_\alpha) - 1][x_A\eta^\alpha_A + x_B\eta^\alpha_B + (1 - x_A - x_B)\eta^\alpha_C] + P(\phi_\beta)[x_A\eta^\beta_A + x_B\eta^\beta_B + (1 - x_A - x_B)\eta^\beta_C] + \tilde{W}_{\alpha\beta}\phi^2_\alpha\phi^2_\beta\} - \left\{ (\eta^\gamma_A - \eta^\gamma_C) + \tilde{V}\ln\left(\frac{x_A}{1 - x_A - x_B}\right)_\alpha + P(\phi_\alpha)(\eta^\alpha_A - \eta^\alpha_C) + P(\phi_\beta)(\eta^\beta_A - \eta^\beta_C)\right\}(x_A - x_A|_\alpha) - \left\{ (\eta^\gamma_B - \eta^\gamma_C) + \tilde{V}\ln\left(\frac{x_B}{1 - x_A - x_B}\right)_\alpha + P(\phi_\alpha)(\eta^\alpha_B - \eta^\alpha_C) + P(\phi_\beta)(\eta^\beta_B - \eta^\beta_C)\right\}(x_B - x_B|_\alpha)\right]\right)^{1/2} d\phi. \tag{B4}$$

with

$$\tilde{\sigma}_{\alpha\beta} = \frac{\sigma_{\alpha\beta}}{\sigma_c}, \quad \tilde{\sigma}_{\alpha\gamma} = \frac{\sigma_{\alpha\gamma}}{\sigma_c}, \quad \tilde{\sigma}_{\beta\gamma} = \frac{\sigma_{\beta\gamma}}{\sigma_c}, \quad \tilde{\delta}_{\alpha\beta} = \frac{\delta_{\alpha\beta}}{\delta_c}, \quad \tilde{\delta}_{\alpha\gamma} = \frac{\delta_{\alpha\gamma}}{\delta_c}, \quad \tilde{\delta}_{\beta\gamma} = \frac{\delta_{\beta\gamma}}{\delta_c}. \tag{B5}$$

The rest have similar forms.

APPENDIX C: COX'S THEORY

Consider two immiscible liquids with viscosity ratio equal to 1. At a leading order in Ca,

$$g(\theta_a) - g(\theta_s) = \mathrm{Ca}\,\ln(\epsilon^{-1}), \tag{C1}$$

where θ_a is the apparent dynamic contact angle, θ_s is the static equilibrium contact angle, ϵ is a very small constant parameter, and the function $g(\theta)$ is given by

$$g(\theta) = \int_0^\theta \frac{d\Theta}{f(\Theta)}, \tag{C2}$$

and

$$f(\theta) = \frac{2\sin\theta\{(\theta^2 - \sin^2\theta) + 2[\theta(\pi - \theta) + \sin^2\theta] + [(\pi - \theta)^2 - \sin^2\theta]\}}{(\theta^2 - \sin^2\theta)[(\pi - \theta) + \sin\theta\cos\theta] + [(\pi - \theta)^2 - \sin^2\theta](\theta - \sin\theta\cos\theta)}. \tag{C3}$$

[1] R. J. Braun, B. T. Murray, W. J. Boettinger, and G. B. McFadden, Phys. Fluids **7**, 1797 (1995).
[2] J. A. Warren, W. J. Boettinger, and A. R. Roosen, Acta Mater. **46**, 3247 (1998).
[3] L. Yin, B. T. Murray, and T. J. Singler, Acta Mater. **54**, 3561 (2006).
[4] E. B. Webb III and G. S. Grest, Scr. Mater. **47**, 393 (2002).
[5] K. Landry, C. Rado, R. Voitovich, and N. Eustathopoulos, Acta Mater. **45**, 3079 (1997).
[6] S. Kalogeropoulou, C. Rado, and N. Eustathopoulos, Scr. Mater. **41**, 723 (1999).
[7] E. Saiz, A. P. Tomsia, and R. M. Cannon, Acta Mater. **46**, 2349 (1998).
[8] E. Saiz, R. M. Cannon, and A. P. Tomsia, Acta Mater. **48**, 4449 (2000).
[9] S. O. Unverdi and G. Tryggvason, J. Comput. Phys. **100**, 25 (1992).
[10] M. Sussman, P. Smereka, and S. Osher, J. Comput. Phys. **114**, 146 (1994).
[11] C. W. Hirt and B. D. Nichols, J. Comput. Phys. **39**, 201 (1981).
[12] D. M. Anderson, G. B. McFadden, and A. A. Wheeler, Annu. Rev. Fluid Mech. **30**, 139 (1998).
[13] J. F. van der Waals, Verh.-K. Ned. Akad. Wet., Afd. Natuurkd., Eerste Reeks **1** (1893) [**20**, 200 (1979)].
[14] C. Huh and L. E. Scriven, J. Colloid Interface Sci. **35**, 85 (1971).
[15] P. Seppecher, Int. J. Eng. Sci. **34**, 977 (1996).
[16] L. Q. Chen and W. Yang, Phys. Rev. B **50**, 15752 (1994).
[17] I. Steinbach, F. Pezzola, B. Nestler, M. Seesselberg, R. Prieler, G. J. Schmitz, and J. L. L. Rezende, Physica D **94**, 135 (1996).
[18] H. Garcke, B. Nestler, and B. Stoth, SIAM J. Appl. Math. **60**, 295 (1999).
[19] J. Tiaden, B. Nestler, H. J. Diepers, and I. Steinbach, Physica D **115**, 73 (1998).
[20] U. Grafe, J. Boettinger, J. Tiaden, and S. G. Fries, Scr. Mater. **42**, 1179 (2000).
[21] J. A. Warren, R. Kobayashi, A. E. Lobkovsky, and W. C. Carter, Acta Mater. **51**, 6035 (2003).
[22] B. Stinner, B. Nestler, and H. Garcke, SIAM J. Appl. Math. **64**, 775 (2004).
[23] B. Nestler, A. A. Wheeler, L. Ratke, and C. Stöcker, Physica D **141**, 133 (2000).
[24] R. F. Sekerka and Z. Bi, in *Interfaces for the Twenty-First Century*, edited by M. K. Smith,M. J. Mixis,G. B. McFadden,G. P. Neitzel, and D. R. Canright(Imperial College Press, London, 2001), pp. 147.
[25] W. J. Boettinger, J. A. Warren, C. Beckermann, and A. Karma, Annu. Rev. Mater. Res. **32**, 163 (2002).
[26] L. Q. Chen, Annu. Rev. Mater. Res. **32**, 113 (2002).
[27] F. Domingues Dos Santos and T. Ondarcuhu, Phys. Rev. Lett. **75**, 2972 (1995).
[28] S. W. Lee, D. Y. Kwok, and P. E. Laibinis, Phys. Rev. E **65**, 051602 (2002).
[29] U. Thiele, K. John, and M. Bär, Phys. Rev. Lett. **93**, 027802 (2004).
[30] K. Asp and J. Ågren, Acta Mater. **54**, 1241 (2006).
[31] W. Villanueva and G. Amberg, Int. J. Multiphase Flow **32**, 1072 (2006).
[32] S.-L. Wang, R. Sekerka, A. Wheeler, B. Murray, S. Coriell, R. Braun, and G. McFadden, Physica D **69**, 189 (1993).
[33] R. Folch and M. Plapp, Phys. Rev. E **72**, 011602 (2005).
[34] D. Jacqmin, J. Comput. Phys. **155**, 96 (1999).
[35] I. Loginova, J. Ågren, and G. Amberg, Acta Mater. **51**, 1327 (2003).
[36] J. W. Cahn and J. E. Hilliard, J. Chem. Phys. **28**, 258 (1958).
[37] G. Amberg, R. Tönhardt, and C. Winkler, Math. Comput. Simul. **49**, 257 (1999).
[38] J. –L. Guermond and L. Quartapelle, in *Proceedings of the 9th International Conference on Finite Elements in Fluids*, Venezia, Italy, 1995, edited by M. Morandi Cecchi,K. Morgan,J. Periaux,B. A. Schrefler, and O. C. Zienkiewicz (SM Legatoria Padova, Venezia, 1995).
[39] P. Shen, H. Fujii, T. Matsumoto, and K. Nogi, Scr. Mater. **49**, 563 (2003).
[40] R. Voitovitch, A. Mortensen, F. Hodaj, and N. Eustathopoulos, Acta Mater. **47**, 1117 (1999).
[41] P. G. de Gennes, F. Brochard-Wyart, and D. Quéré, *Capillarity and Wetting Phenomena* (Springer-Verlag, New York, 2004).
[42] R. G. Cox, J. Fluid Mech. **168**, 169 (1986).
[43] B. Zhou and A. Powell, J. Membr. Sci. **268**, 150 (2006).
[44] See http://www.thermocalc.com
[45] See http://rsb.info.nih.gov/ij/